Discovery of Magnetic Single- and Triple-q States in Mn/Re(0001)

Jonas Spethmann,[1] Sebastian Meyer,[2] Kirsten von Bergmann,[1] Roland Wiesendanger,[1] Stefan Heinze,[2] and André Kubetzka[1,*]

[1]Department of Physics, University of Hamburg, 20355 Hamburg, Germany

[2]Institute of Theoretical Physics and Astrophysics, University of Kiel, Leibnizstrasse 15, 24098 Kiel, Germany

(Received 21 February 2020; accepted 13 May 2020; published 5 June 2020)

We experimentally verify the existence of two model-type magnetic ground states that were previously predicted but so far unobserved. We find them in Mn monolayers on the Re(0001) surface using spin-polarized scanning tunneling microscopy. For fcc stacking of Mn the collinear row-wise antiferromagnetic state occurs, whereas for hcp Mn a three-dimensional spin structure appears, which is a superposition of three row-wise antiferromagnetic states known as the triple-**q** state. Density-functional theory calculations elucidate the subtle interplay of different magnetic interactions to form these spin structures and provide insight into the role played by relativistic effects.

DOI: 10.1103/PhysRevLett.124.227203

In nanoscale noncollinear magnetic systems, various magnetic interactions can compete, ranging from isotropic Heisenberg exchange over spin-orbit coupling (SOC) related effects such as the Dzyaloshinskii-Moriya interaction to recently proposed interactions arising from topological orbital moments. The Heisenberg exchange interaction is described by a symmetric bilinear term of the form $-J_{ij}(\mathbf{S}_i \cdot \mathbf{S}_j)$, with the exchange constant J_{ij} giving the strength of the interaction between spins $\mathbf{S}_i$ and $\mathbf{S}_j$. From the general form of the exchange tensor, other pairwise interactions can be derived, namely, the antisymmetric Dzyaloshinskii-Moriya interaction (DMI) and the anisotropic symmetric exchange (ASE), which both are relativistic effects arising from spin-orbit coupling [1–4]. The DMI has the form $-\mathbf{D}_{ij}(\mathbf{S}_i \times \mathbf{S}_j)$ and thus favors noncollinear magnetic order with unique rotational sense. The ASE can be written as $-J_{ij}^{\mathrm{ASE}}(\mathbf{S}_i \cdot \mathbf{d}_{ij})(\mathbf{S}_j \cdot \mathbf{d}_{ij})$, where $\mathbf{d}_{ij}$ is the unit vector pointing from $\mathbf{S}_i$ to $\mathbf{S}_j$ [3]; because this term describes the anisotropic part of dipolar interactions, the ASE is also referred to as a pseudodipolar interaction. Whereas DMI-induced noncollinear magnetic order has been in the focus of recent research on domain walls and skyrmions [5–7], the ASE is rarely taken into account to model experimental systems [8].

Beyond the pairwise magnetic exchange couplings, also higher-order interactions (HOIs) between four spins have been considered [9], and in several systems their importance for the magnetic ground state has been demonstrated in combined experimental and theoretical studies [10–13]. Recently, additional interactions have been proposed for transition metals, e.g., higher-order DMI [14,15] and interactions involving topological orbital moments arising when the solid angle of three adjacent spins is nonzero [16–19].

When magnetic interactions compete, even structurally simple systems can host complex magnetic states with exciting new properties. In this respect hexagonal magnetic monolayers can serve as auspicious model-type systems. For such a symmetry, antiferromagnetic (AFM) nearest-neighbor exchange coupling leads to geometric frustration and the ground state is a Néel state with 120° between adjacent magnetic moments [20–22]. When exchange interactions beyond nearest-neighbor AFM exchange play a role, e.g., when $1 > J_2/J_1 > 1/8$, the row-wise antiferromagnetic (RW-AFM) state can arise [23,24]. The RW-AFM and the Néel state can both be expressed as spin spirals characterized by a single spin spiral vector **q**.

Within the Heisenberg model, the RW-AFM state is degenerate with the so-called triple-**q** (3Q) state, which can be constructed by a superposition of three symmetry-equivalent RW-AFM states. However, HOIs can lift this degeneracy and favor one state over the other. Nearly two decades ago, the 3Q state was predicted based on density-functional theory (DFT) calculations for a Mn monolayer on Cu(111) [23], but the experimental realization of this system suffered from severe intermixing. Recent calculations for an unsupported Mn layer with a 3Q state indicate sizable topological orbital moments [18] that could lead to additional chiral-chiral and spin-chiral interactions [19]. To the best of our knowledge, neither the RW-AFM state nor the 3Q state have been discovered experimentally up to now.

Here we study the magnetic ground states of Mn monolayers on Re(0001). Using spin-polarized (SP) STM, we find that the RW-AFM state occurs in fcc-stacked Mn, whereas the hcp-stacked Mn exhibits the 3Q state. This is unexpected since the stacking affects only the hybridization of the Mn layer with the second substrate layer. Within DFT calculations, the RW-AFM and the 3Q state are nearly degenerate in both stackings, which allows small effects to promote

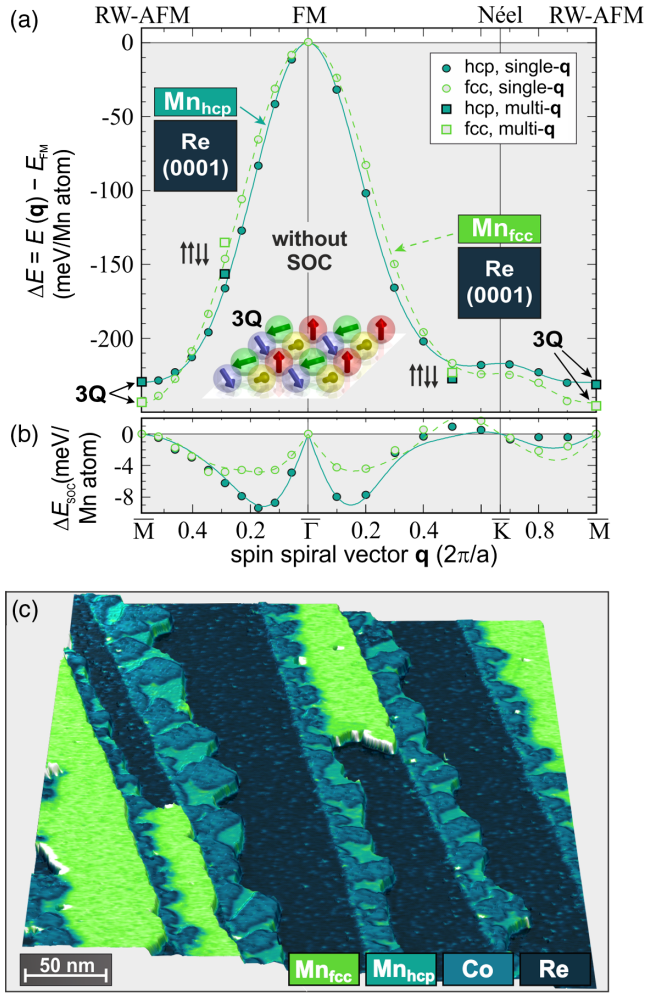

FIG. 1. (a) Energy dispersion $E(\mathbf{q})$ of spin spirals obtained via DFT along the two high symmetry directions of the two-dimensional Brillouin zone for both stackings of Mn on Re(0001) without spin-orbit coupling. The energies of three multi-$\mathbf{q}$ states (3Q and two $\uparrow\uparrow\downarrow\downarrow$) are indicated at the $\mathbf{q}$ vector of the corresponding single-$\mathbf{q}$ state. (b) Calculated energy contribution to spin spirals due to spin-orbit coupling. (c) Perspective view of a constant-current STM topography image of Mn on Re(0001) colorized with the simultaneously acquired differential conductance (dI/dU) signal. Co, decorating the Re step edges, has induced hcp Mn growth [25]; Cr tip, $U = +500$ mV, $I = 1.2$ nA, $T = 4$ K.

one state over the other. The experiments show rotational domains and preferred spin orientations of both magnetic states with respect to the crystallographic directions. To understand the origin of this coupling, we consider different energy contributions such as dipole-dipole interaction and spin-orbit-induced ASE.

In order to scan a large part of the magnetic phase space, we calculate via DFT the energy dispersion $E(\mathbf{q})$ of spin spiral states [Fig. 1(a)], which are the general solutions of the Heisenberg model on a periodic lattice. For a spin spiral characterized by $\mathbf{q}$, i.e., a single-$\mathbf{q}$ state, the magnetic moment of an atom at site $\mathbf{R}_i$ is given by

TABLE I. Calculated values (in meV) for Heisenberg exchange constants J_1'–J_3', where the prime denotes that the effect of higher-order exchange interactions is taken into account in the fit of the energy dispersion, the higher-order exchange constants B_1, Y_1, and K_1, and the energy difference $\Delta E = E_{3Q} - E_{\mathrm{RW-AFM}}$ in meV/Mn atom, neglecting SOC [25].

	J_1'	J_2'	J_3'	B_1	Y_1	K_1	ΔE
fcc	−22.4	−3.4	0.88	−1.56	−2.29	−0.43	−0.7
hcp	−18.7	−4.2	−1.38	−1.25	−2.49	−0.66	−0.4

$\mathbf{M}_i = M(\cos\mathbf{q}\cdot\mathbf{R}_i, \sin\mathbf{q}\cdot\mathbf{R}_i, 0)$, where M is the magnetic moment. For Mn/Re(0001) we find $M_{\mathrm{Mn}} \approx 3.3\ \mu_B$, a value nearly independent of $\mathbf{q}$. The ferromagnetic (FM) state at the $\bar{\Gamma}$ point has a much higher energy compared to the antiferromagnetic 120° Néel state ($\bar{\mathrm{K}}$ point) and the RW-AFM state ($\bar{\mathrm{M}}$ point). For both the fcc- and hcp-stacked Mn monolayer, the RW-AFM state is the lowest energy state of all single-$\mathbf{q}$ states and the fcc stacking of Mn is preferred over hcp Mn by 27.4 meV/Mn atom [25]. By mapping these DFT energy dispersions to the Heisenberg model, we obtain the exchange constants. We find that both nearest- and next-nearest-neighbor coupling, J_1 and J_2, are antiferromagnetic, with a ratio expected for a RW-AFM state [24] (see Table I [25]).

To elucidate whether a 3Q state can occur in Mn/Re (0001), we calculate its total energy with respect to the RW-AFM state. We find that the 3Q state is slightly favored for both stackings due to HOIs (see Table I), with $|\Delta E| < 1$ meV/Mn atom, while in an unsupported Mn monolayer with Re lattice constant the RW-AFM state is strongly favored, with $\Delta E = +21$ meV/Mn atom. The respective values for Mn/Cu(111) are −17 and −15 meV/Mn atom [23]; i.e., the 3Q state is the ground state, independent of the proximity of the Cu(111) surface. This comparison shows that in Mn/Re(0001) an interplay of atomic distance and hybridization with the partly filled 5d band of the Re substrate is crucial for the near degeneracy of the RW-AFM and 3Q state.

The small energy differences do not indicate that the HOIs are negligible. We determine the strength of the two-site (B_1), three-site (Y_1), and four-site (K_1) four spin interaction by calculating in addition the total energy of the two different double-row-wise AFM ($\uparrow\uparrow\downarrow\downarrow$) states [9,12,13,24] with respect to the corresponding single-$\mathbf{q}$ states [25], i.e., 90° spin spirals [see Fig. 1(a)]. The obtained values of B_1, Y_1, and K_1 are of significant strength, see Table I, but their net contribution to the energy of the 3Q and the RW-AFM state nearly cancels.

Spin-orbit coupling effects might also contribute to the formation of the magnetic ground state. The calculated energy contribution due to SOC for cycloidal spin spirals is shown in Fig. 1(b). We find that it is large near $\bar{\Gamma}$, which corresponds to the large DMI reported previously [39].

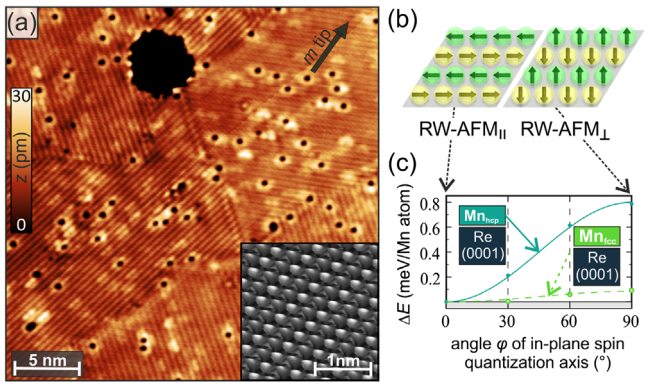

FIG. 2. (a) Spin-resolved constant-current STM image of the fcc-stacked Mn monolayer showing three types of rotational domains of the RW-AFM state. The depicted tip magnetization is based on the different contrast amplitudes assuming RW-AFM$_{\parallel}$ domains. Fe-coated W tip, $U = -20$ mV, $I = 7.5$ nA, $T = 8$ K, $B = 0$ T, raw data. The atom manipulation image (inset) demonstrates commensurability of magnetic state and atomic lattice (Co adatom, Cr tip, $U = 5$ mV, $I = 4$ nA). (b) Spin structures of RW-AFM states with spin quantization axes parallel and perpendicular to the rows. (c) DFT calculation of the energy of in-plane RW-AFM states as a function of the angle of the spin quantization axis.

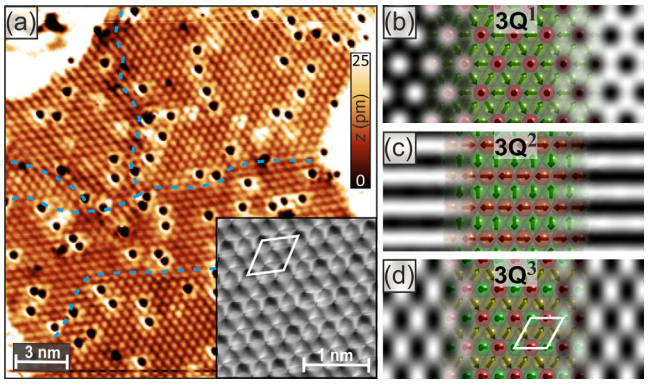

FIG. 3. (a) Spin-resolved constant-current STM image of the hcp-stacked Mn monolayer showing three types of rotational domains of the $3Q^3$ state. Domain boundaries are indicated [25]; Cr tip, $U = -30$ mV, $I = 7$ nA, $T = 4$ K, $B = 0$ T, raw data. (Inset) The commensurability of the 3Q state is demonstrated by atom manipulation (Co adatom, Cr tip, $U = 5$ mV, $I = 10$ nA). (b)–(d) Spin structures (red, up; green, down) and SP-STM simulations of three differently oriented $3Q^i$ states, with tip magnetization pointing up (left side) and down (right side).

However, its impact is significantly reduced at $\bar{\mathrm{M}}$, i.e., close to the RW-AFM state. We find for both stackings of the Mn an easy-plane magnetocrystalline anisotropy energy (MAE) on the order of 1 meV/Mn atom. The MAE favors the RW-AFM state over the 3Q state and changes their energy difference ΔE given in Table I by about $+0.3$ meV/Mn atom [25]. So far, the DFT results demonstrate a competition of different types of interactions, preventing a robust prediction of the magnetic ground states.

In the experiment, Mn grows on Re(0001) almost exclusively in fcc stacking [25], in agreement with the DFT calculations. Extended areas of hcp Mn can be induced by previously growing Co, which decorates the Re step edges, as can be seen in Fig. 1(c), where hcp and fcc Mn areas coexist. Figure 2(a) shows a closer view of a fcc Mn monolayer area, grown without Co. Here, a spin-sensitive Fe-coated W tip is used, which is typically sensitive to the in-plane components of the sample magnetization in zero field [40]. We observe three rotational domains of stripes running along the close-packed atomic rows. The distance between the stripes is exactly two atomic rows as inferred from magnetic atom manipulation imaging (see Supplemental Material [25]), and thus we conclude that fcc Mn exhibits the RW-AFM state. Different rotational domains can show different magnetic contrast amplitudes, e.g., the contrast is lowest for the domain in the upper right. An out-of-plane easy axis would result in the same contrast independent of the rotational domain and can therefore be excluded, in agreement with the easy-plane MAE obtained from DFT. Furthermore, we find a strong correlation of AFM row direction and magnetic corrugation amplitude—in these data and in general—with almost no exceptions. This means that the spin direction is coupled to the magnetic rows of the AFM state in one of the two ways depicted in Fig. 2(b).

Surprisingly, none of the previously considered interactions, i.e., Heisenberg exchange, HOIs, MAE, or DMI, can mediate this kind of coupling. However, so far we have—as often reasonable for ultrathin films and antiferromagnets—neglected the magnetic dipole-dipole interaction. We can calculate its energy contribution for the two states based on the magnetic moment of 3.3 μ_B per Mn atom as obtained from DFT. Thereby, we find that the configuration with spin quantization axis parallel to the rows, RW-AFM$_{\parallel}$, is favored by 0.14 meV/Mn atom compared to RW-AFM$_{\perp}$, a value roughly 2/3 of the shape anisotropy of a FM state.

In addition to the dipolar contribution, the spin-orbit-coupling-induced ASE can lead to an energy difference between the two configurations. We can quantify this effect for both stackings with DFT by calculating the energy of the RW-AFM state for different rotations of the spin quantization axis with respect to the direction of the rows, see Fig. 2(c). We find that in fcc Mn the ASE leads to an energy difference of about 0.1 meV/Mn atom, with a preference for the RW-AFM$_{\parallel}$ state. The dipole-dipole interaction and the ASE are thus of similar strength and both mediate a spin orientation along the AFM rows.

Figure 3(a) shows a spin-resolved STM image of hcp Mn monolayer and adjacent Co areas (white), imaged with a Cr tip, which can have an arbitrary magnetization direction. We observe a hexagonal superstructure with twice the atomic lattice constant, i.e., four atoms in the magnetic unit cell as found from magnetic atom manipulation imaging (see Supplemental Material [25]), compatible with the

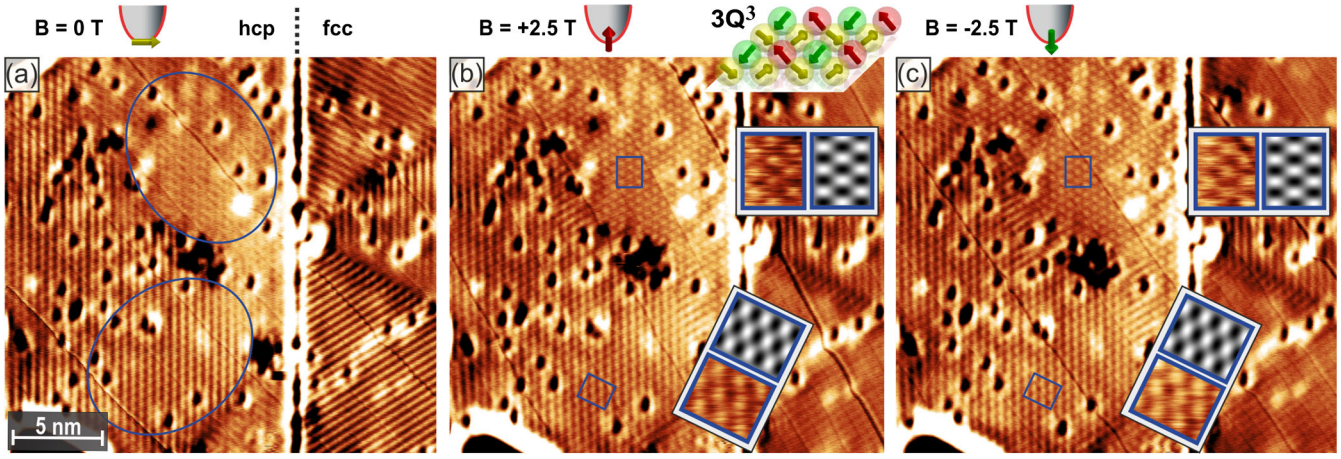

FIG. 4. Spin-resolved STM images of hcp and fcc Mn areas with different tip magnetization directions sensitive to (a) in-plane and (b),(c) opposite out-of-plane sample magnetization components; Fe-coated W tip, $U = -30$ mV, $I = 7$ nA, $T = 8$ K, partially differentiated constant-current images [25]; straight diagonal lines are digital feedback artifacts. Insets in (b) and (c) show enlarged raw data views of the indicated areas together with SP-STM simulations (gray scale) of the $3Q^3$ state sketched above, where yellow spins are fully in plane.

presence of a 3Q state. In different regions of the Mn monolayer, the details of the hexagonal pattern change and we find three qualitatively different regions in Fig. 3(a), indicating rotational domains analogous to the RW-AFM domains in Fig. 2(a). Since SP-STM is sensitive to the projection of surface spins onto the tip magnetization [40], the observed patterns depend on the 3Q rotational domain as well as the tip magnetization direction [25,41,42].

In the ideal 3Q state all adjacent spins span angles of $\tau = \arccos(-1/3) \approx 109.47°$ (tetrahedron angle). In a monolayer, there can be different orientations of 3Q states with respect to the plane and also different permutations of the atoms among the different sites. Three highly symmetric versions, denoted $3Q^i$, $i = 1, 2, 3$, are depicted in the centers of Figs. 3(b)–3(d), where the color indicates the out-of-plane magnetization component. They can be transformed into one another by rotating all spins, i.e., $\tau/2$ from $3Q^1$ to $3Q^2$ and 90° from $3Q^2$ to $3Q^3$. To the sides are SP-STM simulations based on a simplified model [42] assuming opposite out-of-plane tip magnetization directions. For $3Q^1$ two rotational domains exist that cannot be distinguished with an out-of-plane tip, while an inverted pattern is observed when either tip or sample magnetization is inverted. Both orientations $3Q^2$ and $3Q^3$ are uniaxial and three rotational domains are expected. Upon a tip or sample magnetization inversion [cf. Figs. 3(c) and 3(d)], the magnetic pattern of these states is preserved but shows a phase shift in the simulation.

Experimentally we can measure different magnetization components at the same sample position exploiting the field dependence of an Fe-coated W tip (see schematics at the top of Fig. 4). The spin moments of 3Q and RW-AFM state are fully compensated on the atomic scale and should therefore not react to moderate external magnetic fields. Figure 4(a) shows a sample area with hcp Mn monolayer on the left side and fcc Mn monolayer on the right side of a dislocation line, measured with an in-plane sensitive tip. Two hcp Mn areas with qualitatively different patterns are indicated, which we interpret as different rotational domains of the 3Q state. When the tip is sensitive to the out-of-plane magnetization component, see Figs. 4(b) and 4(c), the observed magnetic pattern changes and both areas look more similar [25]. Close inspection of the data reveals that the two patterns exhibit a phase shift upon tip magnetization inversion, and we find that the pattern shifts in different directions for the two magnetic domains. This is best seen in the insets in Figs. 4(b) and 4(c), where the raw data from the indicated areas are compared to simulated SP-STM images (gray) of the $3Q^3$ state depicted above. While the $3Q^1$ and $3Q^2$ orientations are inconsistent with these data [cf. Figs. 3(b) and 3(c)], the agreement of raw data and simulation indicates that the $3Q^3$ state is realized in hcp Mn.

The question arises as to which magnetic interaction couples the 3Q state to the lattice in this particular way. There is no energy difference between the different $3Q^i$ states when considering Heisenberg exchange, the HOIs, the MAE, or the DMI. An estimation of the dipolar energy for these noncollinear configurations shows that it changes by only 0.01 meV/atom between the different $3Q^i$ states. The value of the ASE in nearest-neighbor approximation can be obtained from the DFT calculations in Fig. 2(c) and for hcp Mn it is $J_1^{\mathrm{ASE}} = \Delta E/4 = 0.2$ meV, which is an order of magnitude stronger compared to fcc Mn. However, because the ASE energy minimizes for collinear spin configurations, it leads to an energy difference between the different $3Q^i$ of only 0.07 meV per Mn atom. While the experimental observations point to the $3Q^3$ state, $3Q^1$ is slightly favored by both the dipolar interaction and the ASE. The estimated total energy difference of the $3Q^1$ and

$3Q^3$ state is about 0.08 meV/Mn atom, a factor of 3 smaller than the difference of RW-AFM$_\parallel$ and RW-AFM$_\perp$ in fcc Mn.

For an improved theoretical description of the 3Q state it may be necessary to consider additional effects. First, rigid tetrahedron angles in the 3Q state might be an oversimplification: slight distortions potentially reduce the energy cost of MAE, ASE, and dipolar contributions and at the same time change the considered HOI energies, which might affect both energy and orientation of the magnetic state. Second, because the considered HOIs nearly cancel, additional higher-order terms might play a decisive role in this system. Moreover, due to the large angles between adjacent spins, the 3Q state carries a significant topological charge of $q = 0.5$ per triangular plaquette or two per magnetic unit cell; for comparison, a skyrmion carries $q = 1$. This can give rise to orbital moments [18] and additional energy contributions from chiral-chiral or spin-chiral interactions [19].

We conclude by emphasizing that two model-type magnetic states have been found experimentally for the first time, and in both cases the orientation of the spin structure couples to the atomic lattice. For the RW-AFM$_\parallel$ state, the dipolar interaction and the anisotropic symmetric exchange can explain this coupling. For the $3Q^3$ state, we find that these two terms are too small to cause the coupling, and other effects such as a distortion of the spin state may be responsible. Complex spin structures such as the 3Q state are promising candidates to induce topological superconductivity [43] below the critical temperature of about 1.7 K of Re and to exhibit interesting transport properties even in the normal conducting state.

K. v. B., S. H., and A. K. acknowledge financial support from the Deutsche Forschungsgemeinschaft (DFG, German Research Foundation) Grants No. 418425860, No. 402843438, and No. 408119516. R. W. acknowledges financial support by the EU via the ERC Advanced Grant ADMIRE. K. v. B. thanks S. Blügel for pointing out references. A. K. thanks L. Rosza for discussions and J. Sassmannshausen for technical support. S. H. and S. M. thank Y. Mokrousov and G. Bihlmayer for discussions and S. Haldar, S. Paul, and M. Goerzen for technical support and acknowledge computing time at the supercomputer of the North-German Supercomputing Alliance (HLRN).

*Corresponding author.
kubetzka@physnet.uni-hamburg.de

[1] I. E. Dzyaloshinskii, Sov. Phys. JETP **5**, 1259 (1957).
[2] T. Moriya, Phys. Rev. **120**, 91 (1960).
[3] D. A. Smith, J. Magn. Magn. Mater. **1**, 214 (1976).
[4] J. B. Staunton, B. L. Gyorffy, J. Poulter, and P. Strange, J. Phys. C **21**, 1595 (1988).
[5] K. von Bergmann, A. Kubetzka, O. Pietzsch, and R. Wiesendanger, J. Phys. Condens. Matter **26**, 394002 (2014).
[6] R. Wiesendanger, Nat. Rev. Mater. **1**, 16044 (2016).
[7] A. Fert, N. Reyren, and V. Cros, Nat. Rev. Mater. **2**, 17031 (2017).
[8] J. Hermenau, S. Brinker, M. Marciani, M. Steinbrecher, M. d. S. Dias, R. Wiesendanger, S. Lounis, and J. Wiebe, Nat. Commun. **10**, 1 (2019).
[9] M. Hoffmann and S. Blügel, Phys. Rev. B **101**, 024418 (2020).
[10] S. Heinze, K. von Bergmann, M. Menzel, J. Brede, A. Kubetzka, R. Wiesendanger, G. Bihlmayer, and S. Blügel, Nat. Phys. **7**, 713 (2011).
[11] Y. Yoshida, S. Schröder, P. Ferriani, D. Serrate, A. Kubetzka, K. von Bergmann, S. Heinze, and R. Wiesendanger, Phys. Rev. Lett. **108**, 087205 (2012).
[12] N. Romming, H. Pralow, A. Kubetzka, M. Hoffmann, S. von Malottki, S. Meyer, B. Dupé, R. Wiesendanger, K. von Bergmann, and S. Heinze, Phys. Rev. Lett. **120**, 207201 (2018).
[13] A. Krönlein, M. Schmitt, M. Hoffmann, J. Kemmer, N. Seubert, M. Vogt, J. Küspert, M. Böhme, B. Alonazi, J. Kügel, H. A. Albrithen, M. Bode, G. Bihlmayer, and S. Blügel, Phys. Rev. Lett. **120**, 207202 (2018).
[14] S. Mankovsky, S. Polesya, and H. Ebert, Phys. Rev. B **101**, 174401 (2020).
[15] S. Brinker, M. d. S. Dias, and S. Lounis, New J. Phys. **21**, 083015 (2019).
[16] M. Hoffmann, J. Weischenberg, B. Dupé, F. Freimuth, P. Ferriani, Y. Mokrousov, and S. Heinze, Phys. Rev. B **92**, 020401(R) (2015).
[17] M. d. S. Dias, J. Bouaziz, M. Bouhassoune, S. Blügel, and S. Lounis, Nat. Commun. **7**, 1 (2016).
[18] J.-P. Hanke, F. Freimuth, A. K. Nandy, H. Zhang, S. Blügel, and Y. Mokrousov, Phys. Rev. B **94**, 121114(R) (2016).
[19] S. Grytsiuk, J.-P. Hanke, M. Hoffmann, J. Bouaziz, O. Gomonay, G. Bihlmayer, S. Lounis, Y. Mokrousov, and S. Blügel, Nat. Commun. **11**, 511 (2020).
[20] D. Wortmann, S. Heinze, P. Kurz, G. Bihlmayer, and S. Blügel, Phys. Rev. Lett. **86**, 4132 (2001).
[21] C. L. Gao, W. Wulfhekel, and J. Kirschner, Phys. Rev. Lett. **101**, 267205 (2008).
[22] S. Ouazi, A. Kubetzka, K. von Bergmann, and R. Wiesendanger, Phys. Rev. Lett. **112**, 076102 (2014).
[23] P. Kurz, G. Bihlmayer, K. Hirai, and S. Blügel, Phys. Rev. Lett. **86**, 1106 (2001).
[24] B. Hardrat, A. Al-Zubi, P. Ferriani, S. Blügel, G. Bihlmayer, and S. Heinze, Phys. Rev. B **79**, 094411 (2009).
[25] See Supplemental Material http://link.aps.org/supplemental/10.1103/PhysRevLett.124.227203 for experimental and computational details, which includes Refs. [26–38].
[26] S. Ouazi, T. Pohlmann, A. Kubetzka, K. von Bergmann, and R. Wiesendanger, Surf. Sci. **630**, 280 (2014).
[27] A. Palacio-Morales, A. Kubetzka, K. von Bergmann, and R. Wiesendanger, Nano Lett. **16**, 6252 (2016).
[28] B. Wolter, Y. Yoshida, A. Kubetzka, S.-W. Hla, K. von Bergmann, and R. Wiesendanger, Phys. Rev. Lett. **109**, 116102 (2012).
[29] J. A. Stroscio and R. J. Celotta, Science **306**, 242 (2004).
[30] https://www.flapw.de.
[31] D.-P. Ji, Q. Zhu, and S.-Q. Wang, Surf. Sci. **651**, 137 (2016).

[32] J. P. Perdew, K. Burke, and M. Ernzerhof, Phys. Rev. Lett. **77**, 3865 (1996).
[33] P. Kurz, F. Förster, L. Nordström, G. Bihlmayer, and S. Blügel, Phys. Rev. B **69**, 024415 (2004).
[34] S. H. Vosko, L. Wilk, and M. Nusair, Can. J. Phys. **58**, 1200 (1980).
[35] M. Heide, G. Bihlmayer, and S. Blügel, Physica (Amsterdam) **404B**, 2678 (2009).
[36] S. Meyer, B. Dupé, P. Ferriani, and S. Heinze, Phys. Rev. B **96**, 094408 (2017).
[37] B. Zimmermann, G. Bihlmayer, M. Böttcher, M. Bouhassoune, S. Lounis, J. Sinova, S. Heinze, S. Blügel, and B. Dupé, Phys. Rev. B **99**, 214426 (2019).
[38] S. Paul, S. Haldar, S. von Malottki, and S. Heinze, arXiv: 1912.03474v2.
[39] A. Belabbes, G. Bihlmayer, F. Bechstedt, S. Blügel, and A. Manchon, Phys. Rev. Lett. **117**, 247202 (2016).
[40] M. Bode, Rep. Prog. Phys. **66**, 523 (2003).
[41] D. Wortmann, P. Kurz, S. Heinze, K. Hirai, G. Bihlmayer, and S. Blügel, J. Magn. Magn. Mater. **240**, 57 (2002).
[42] S. Heinze, Appl. Phys. A **85**, 407 (2006).
[43] S. Nakosai, Y. Tanaka, and N. Nagaosa, Phys. Rev. B **88**, 180503(R) (2013).